Preserved layered structure enables stable cyclic performance of MoS_2 upon potassium insertion

Xiaoqiong Du, ‡ Jiaqiang Huang, ‡ Xuyun Guo, Xiuyi Lin, Jian-Qiu Huang, Hong Tan, Ye Zhu, Biao Zhang*

Department of Applied Physics, The Hong Kong Polytechnic University, Hung Hom, Hong Kong, PR China.

Corresponding Author

*E-mail address: biao.ap.zhang@polyu.edu.hk (Biao Zhang)

‡These authors contributed equally to this work.

K-ion batteries; MoS_2 phase transition; intercalation; conversion; stability.

ABSTRACT: Transitional metal dichalcogenides represent one important type of anodes for emerging K-ion batteries. K ions are stored through both intercalation and conversion reactions, but the detailed phase transition is not clear. It is believed that deep potassiation would trigger the conversion reaction, which induces the fracture of particles and lead to fast capacity degradation. Utilizing MoS_2 as a model material, the competition between intercalation and conversion is revealed, which shows a rate-dependent behavior. The crystal structure of several newly discovered intermediate phases including $K_{0.5}MoS_2$ and $K_{1.0}MoS_2$ is disclosed by complementary experimental and calculational approaches. It shows that intercalation takes place even discharge down to 0 V, differing from the cases in Li-ion and Na-ion batteries. The intercalated compound preserves the layered structure of MoS_2, which avoids the structural collapse and maintains the integrity of the electrode for stable cyclic performance. This finding opens up a new opportunity in the exploration of high capacity anode among layered transitional metal dichalcogenide families.

1. Introduction

Research on K-ion batteries (KIBs) has been revived in recent years[1-6]. The abundance of potassium element in earth renders the forthcoming KIBs considerable advantage in sustainability over Li-ion batteries, which are afflicted by the limited lithium reserve.[7] Nevertheless, the large radius of K ions brings about the difficulty in designing appropriate electrode materials for attaining competitive energy densities. The similarities between the alkali-metal ion intercalation chemistry greatly facilitate the screening of promising compounds.[8] The reported several candidate cathodes, such as $K_{0.7}CrO_2$ layered oxide, $K_3V_2(PO_4)_2F_3$ polyanion and KFeMnCN Prussian blue, are inherited from the analogs in Li-ion and Na-ion batteries[9-11]. These cathodes have delivered attractive performance in both energy density and rate performance. Turning to the anodes, studies are focused on three major categories including intercalation, alloy and conversion electrodes[12-13]. In general, the intercalation anodes such as graphitic carbon and $K_2Ti_4O_9$ deliver more stable cyclic performance than the latter two types, due to less strain during potassiation.[14-15] However, alloy and conversion anodes, such as Bi, Sb, and transition metal dichalcogenides (TMDs), could uptake more K ions for gaining high capacities. [16-20]

TMDs like MoS_2, $MoSe_2$, TiS_2, VSe_2 and ReS_2, store the K ions making use of conversion reactions to a large extent.[21-27] Up to four K ions could be uptake, giving rise to a theoretical capacity of over two times as that of a graphite anode, but also cause the capacity degradation arising from enormous strains in the electrode.[28] To alleviate the large volume change during K ion insertion, nanostructured electrodes are widely fabricated, in particular, with nanocarbon materials incorporation.[29-32] Thanks to these efforts, the capacity retention is significantly improved, but some issues associated with nanomaterials, including the low tap density and large irreversible capacity, remain challenging. Parallel studies on engineering the solid electrolyte interphase (SEI) are conducted to build elastic SEIs for accommodating the volume expansion and maintaining the integrity of the electrode.[33-35] The strategy has been proven effective in stabilizing the anodes of both Na-ion batteries and KIBs with the utilization of glyme-based electrolyte,[19,36] although their practical application is restricted by the narrow electrochemical window of glyme solvent compared to carbonate.[37-39]

In addition to the electrode morphology and interphase structure, the cyclic stability also relies largely on the insertion chemistry. Understanding on the phase transition of metal dichalcogenides during K ions insertion is mainly deduced from their lithiation and sodiation processes.[40-41] Although alkali-metal ion insertion chemistry shares many similarities, prudent exploration is required since a simple extrapolation has proven to be not enough in many cases. In general, both intercalation and conversion take place during potassiation,[23-24,42] but the detailed process is still a mystery, which also brings about the difficulty in analyzing the corresponding electrode stability. An interesting work by Wu's group is to utilize only the K ion intercalation but avoid the conversion of MoS_2 through shallow discharge to 0.5 V vs. K/K^+, where an intercalated compound $K_{0.4}MoS_2$ is formed.[43] It shows super-stable cyclic performance because of intercalation-only behavior. Nevertheless, the capacity is limited to 67 mA h g^{-1} due to a merely 0.4 K ion intercalation. The detailed phase transition beyond x>0.4 in K_xMoS_2 is not clear. It is believed that deep discharge will trigger the fully conversion of MoS_2 into Mo and K_2S, leading to the collapse of layered structure with associated rapid capacity fading. In the current study, using the micro-sized MoS_2 as a model material, we unveil the phase competition between the intercalation and conversion, which shows a rate-dependent reaction path and has significant implication on the cyclic stability.

2. Experimental Section

2.1 Material and methods

Commercial molybdenum disulfide (powder, <2um, 99%) were purchased from Sigma Aldrich. MoS_2 powder, vapor grown carbon fibers (VGCF), super P and carboxymethyl cellulose (CMC) with a mass ratio of 7: 1: 1: 1 in weight were mixed by ball milling for 2 hours. A uniform slurry was prepared by dispersed the mixture in deionized water. Then the as-prepared slurry was coated on Cu foil to make a tape. After being dried 80 °C for 12 hours, MoS_2 electrodes with a diameter of 12 mm were used to assemble coin cell and Swagelok type cell.

2.2 Materials characterization

The XRD patterns were collected by Rigaku Smartlab with Cu-Kα radiation source at 45 kV and 200 mA condition. XRD cell holder with a beryllium window was employed to perform in situ tests where the sample was coated on beryllium window without Cu foil. Ex situ XRD measurements was conducted with Swagelok type cells. The samples that coated on Cu current collector at different discharge and charge states were collected. The cells were disassembled in the glovebox and washed with dimethyl carbonate (DMC). All TEM and STEM were performed using JEOL JEM-2100F TEM/STEM operated at 200 kV, which is equipped with Oxford INCA EDS detector. STEM images were taken with a 13 mrad convergence angle for the optimal probe condition. The sample was firstly fabricated on a TEM grid in a glovebox with an inert Ar atmosphere and then sealed into an argon-filled apparatus before taking out into ambient air. Just before the observation, the sealed bag was cut opened and then the sample was transferred to a double-tilt beryllium holder (JEOL). All Batteries were tested on LAND battery or Arbin system. In situ Raman spectra were obtained by WITec alpha 300 confocal Raman microscope (532 nm laser excitaion) with EL CELL type cell. XPS spectra were obtained on Physical Electronic PHI5600 machine (Al target).

2.3 Electrochemical measurements

All cells were assembled via two-electrode coin half cell (CR2032) in the Argon-filled glovebox with 1 M potassium bis(fluorosulfony)imide (KFSI) in ethylene carbonate (EC)/ propylene carbonate (PC) as electrolyte and glass fiber membranes as separators. The volume ratio of EC and PC is 1: 1. The MoS_2 electrode served as an anode and metallic potassium was utilized as a counter/reference electrode. XRD cell and EL CELL type cell were also assembled by the same way.

2.4 DFT Calculations

DFT calculations were carried out with generalized gradient approximation parameterized by Perdew-Burke-Ernzerhof performed in the Vienna Ab initio Simulation Package[44-46]. The optimized Perdew, Burke, and Ernzerhof functional (opt-PBE) were utilized for van der Waals interactions, due to the better consistence in the case of MoS_2 (**Table S1**).[47] An energy cut-off of 500 eV was adopted, and the k-point was sampled limiting the spacings <0.05 $Å^{-1}$. The energy and force convergence criteria were 10^{-6} eV and 0.02 eV $Å^{-1}$, respectively. Spin polarization was considered. When the energies of phases are <10 meV per atom above the convex hull or just on the hull, they were regarded as the thermodynamically stable structures within DFT and temperature errors.[48] The equilibrium potentials were calculated according to the following equation:

$$nK^+ + ne^- + MoS_2 \rightarrow K_nMoS_2 \quad (1)$$

$$U = \frac{\Delta G}{-ne} = \frac{E(K_nMoS_2) - nE(K) - E(MoS_2)}{-ne} \quad (2)$$

where n is the number of electrons involved in the reaction, U is the equilibrium potential of the reaction, $E(K_nMoS_2)$, E(K), and $E(MoS_2)$ represent the computed total energies of K_nMoS_2, K, and MoS_2 at 0 K by DFT, respectively.

3. Results and Discussion

Commercial MoS_2 were directly used as active materials. The microsized MoS_2 is not only beneficial to achieving high Coulombic efficiency and tap density in batteries but also has better crystallinity for high quality structural examination than nanosized counterpart. SEM images in **Figure S1** shows the average particle size is around 1.43 μm. They were mixed with 10% carbon super P (SP), 10% vapor grown carbon fibres (VGCF) and 10% carboxymethyl cellulose (CMC) binder to prepare the electrode. 1 M KFSI in EC/PC were adopted as an electrolyte since KFSI salt has been proven beneficial in forming SEI.[49-50] The voltage profiles of the cell cycled at 50 mA g^{-1} are given in **Figure 1**a. Three plateaus located at 1.06, 0.36 and 0. 09 V are observed in the first discharge, as seen from the dQ/dV curve (Figure 1b), with an accumulative capacity of 537 mA h g^{-1}. In comparison, the charge profile consists of a sloping curve below 1.2 V and a plateau at around 1.56 V with a total capacity of 405 mA h g^{-1}, corresponding to an initial Coulombic efficiency of 75%. The large capacity loss is mainly ascribed to the formation of SEI. The efficiency could be increased with less amount of carbon SP (Fig. Sx). A dense SEI layer with a thickness of around 25 nm is coated on the MoS_2 particles as shown in **Figure S2**a. It is composed of several organic species such as O-C=O plus inorganic particles

including K_2O_2/KOH as deduced from XPS result in Figure S2b.

The subsequent discharge curve differs a lot from the initial one, which is absent from any clear plateaus and only displays a sloping feature. It indicates a different K storage mechanism after initial potassiation. The profiles of the following cycles have identical shapes with the 1st charge and 2nd discharge ones. The capacity becomes stable starting from the 3rd cycle as can be seen in Figure 1c. It is a surprise that the capacity does not decrease much when the current density increases from 50 mA g^{-1} to 1000 mA g^{-1}. The low-rate cycling enables the enlargement of d-spacing, facilitating the K ion transfer under high-current rates as will be discussed later. A capacity of 302 mA h g^{-1} is maintained when cycled at 1000 mA g^{-1}. It suggests a fast K ion diffusion in MoS_2, which is confirmed in the galvanostatic intermittent titration technique (GITT) results (Figure 1d and **Figure S3**). Despite the varied diffusion coefficient in the first potassiation, which may due to the complex phase transitions as will be discussed later, the following K ions insertion/extraction delivers a stable and high value in the order of 10^{-11} cm^2 s^{-1}. This value is comparable to that in Na ion batteries, although K ion has a larger radius than Na one.[51] Lastly, the capacity is recovered to 380 mA h g^{-1} when the current density reduces to 100 mA g^{-1}, demonstrating superior reversibility. The obtained performance of microsized MoS_2 is among the best in TMDs anode materials (**Figure S4**), even comparable to the nanostructured composites. The excellent cyclic stability in the microsized particles is out of our expectation, which may imply a distinct reaction path and deserve further investigation.

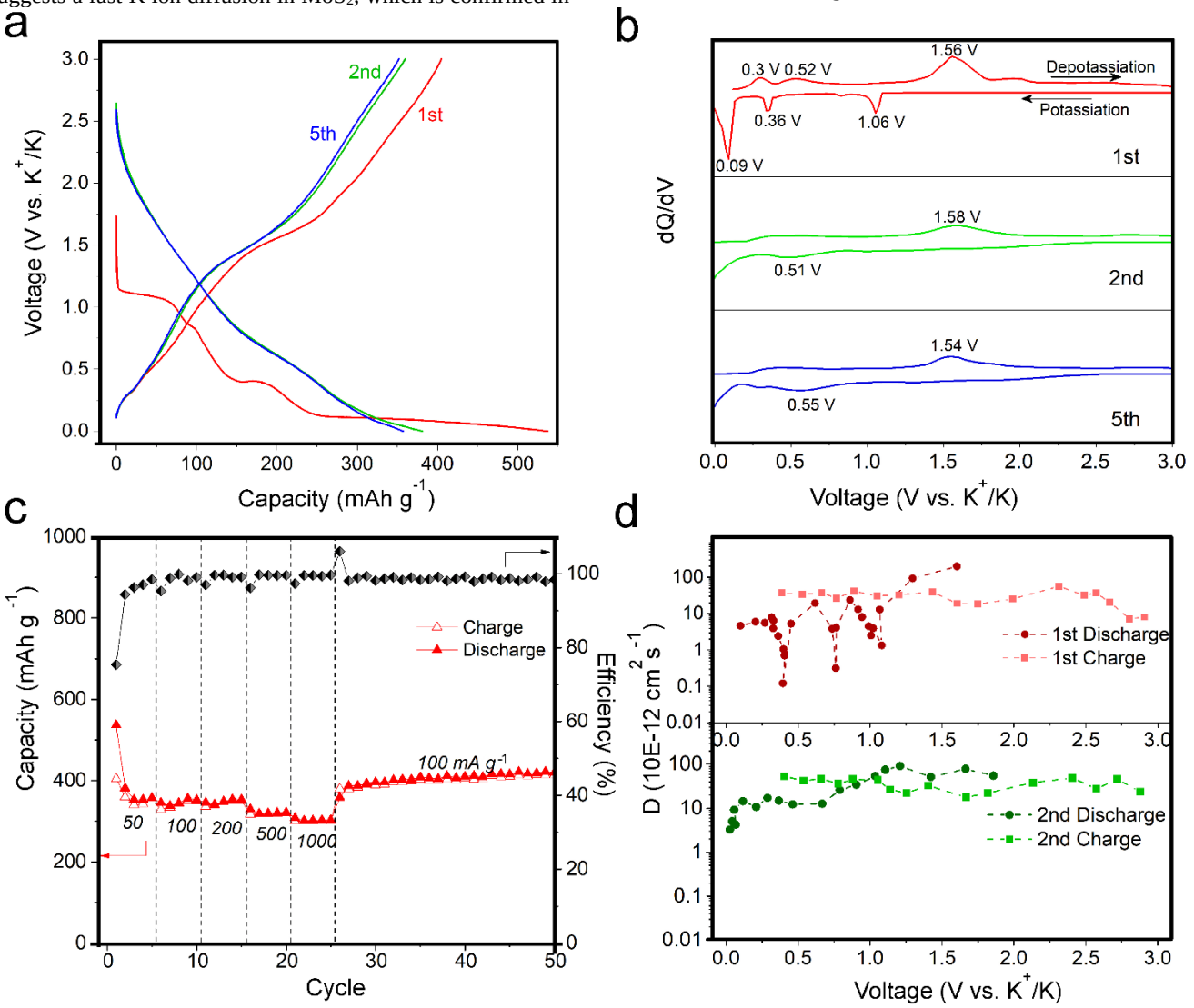

Figure 1 Electrochemical performance of MoS_2 anodes in KIBs. (a)The 1st, 2nd and 5th charge and discharge profiles; (b) the corresponding differential capacity curves (dQ/dV); (c) rate performance, cycling stability and Coulombic efficiency; (d) diffusion coefficients as a function of discharge and charge during the 1st and 2nd cycle.

In situ X-ray diffraction (XRD) was carried out to investigate the phase transition of microsized MoS_2 anodes. A Swagelok-type cell equipped with a Beryllium window was adopted for the test. The cell was cycled between 0 and 3 V at a low current density of 10 mA g^{-1} for fully reaction. Based on the electrochemical curves in Figure 1, the XRD patterns under

different charge/discharge depths during first discharge (D1), first charge (C1) and second discharge (D2) were selected and presented in **Figure 2**a. The pattern at open circuit voltage (OCV) state agrees well with 2H-MoS_2 (PDF#37-1492). Several peaks contributed by conductive carbon and Be window are also observed. 2H-MoS_2 has a layered structure consisting of covalently bonded S-Mo-S layers. The (002) peak of pristine MoS_2 is located at 14.5°, corresponding to a d-spacing of 6.1 Å. Upon discharging to 0.9 V, the (002) peak downshifts to 10.8° together with the appearance of new peaks at 21.6°, which could be assigned to the hexagonal $K_{0.4}MoS_2$ compound. This newly formed compound has an expanded d-spacing of 8.3 Å. The peaks from residual MoS_2 are also observed as an indication of incomplete transition at this stage. With further intercalation of K ions, a slightly right shift of (002) peak from 10.8° to 11.0° is found, which suggests a small shrinkage of the unit cell. The small contraction may result from a distortion of initial 2H structure, leading to the formation of K_yMoS_2. The peak intensity of this phase gradually decreases with continuously discharging, accompanied by the appearance of a broad peak at 11.5° implying the formation of another phase K_zMoS_2 (z>y) at 0.1 V. It is counterintuitive to find that the d-spacing of K_zMoS_2 tends to be reduced with the intercalation of more K ions. Based on previous studies the obvious constriction may attribute to the phase transition from distorted 2H structure to more stable 1T phase, similar to the Li, Na intercalated MoS_2[52-55]. When the cell reaches 0V, the K_yMoS_2 disappears and only the K_zMoS_2 is maintained. Here the accurate value of y and z is difficult to be determined from the capacity due to the possible involvement of conversion reaction and concomitant electrolyte decomposition, hence discouraging ones to reveal the detailed crystal structure of the two phases based solely on the XRD patterns.

To address the above issue, theoretical calculations were conducted to figure out the compounds during the K ion insertion. Figure 2b shows the formation enthalpy of all the feasible potassium intercalated MoS_2 phases from the database and Li analogs.[56-57] It suggests a reaction path of MoS_2-$K_{0.5}MoS_2$-$K_{1.0}MoS_2$-$K_{1.5}MoS_2$ upon potassiation. Apart from the reported $K_{0.4}MoS_2$ phase, the simulated XRD patterns of $K_{0.5}MoS_2$ and $K_{1.0}MoS_2$ agree well with the K_yMoS_2 and K_zMoS_2 phases that observed in the in situ XRD tests (Figure 2c). It reveals that the value of y and z equals to 0.5 and 1, respectively. The K_1MoS_2 is also confirmed by chemical synthesis through ball milling of stoichiometric amount of potassium and MoS_2. $K_{0.5}MoS_2$ and $K_{1.0}MoS_2$ belong to two different phases of 2H and 1T, but with a distortion in the structure. The parameters of the crystal lattice are given in **Table S2**. Lastly, the calculation indicates the presence of $K_{1.5}MoS_2$, which is absent in the experimental results due possibly to its unfavourable kinetics. $K_{1.5}MoS_2$ is not a layered structure anymore (**Figure S5**), which may possess a higher energy barrier to break/form the bonds.

Upon charging, the K ions are removed from $K_{1.0}MoS_2$. Interestingly, the main peak at 11.5° degree gradually shifts to the left as a reflection of d-spacing enlargement. The end-phase when charging to 3V, denoted as K_xMoS_2 (x<1), recovers to neither initial intercalated compound $K_{0.4}MoS_2$ nor pristine MoS_2. In the following K ion intercalation (2nd discharge), the peak shifts back and finally restore to $K_{1.0}MoS_2$ at 0V, suggesting the reversibility of the insertion/extraction process between K_xMoS_2 and $K_{1.0}MoS_2$ after 1st discharge. It is worth noting that a small peak at 14.5° associated with unreacted MoS_2 exists at all the states, due to the incomplete reaction arising from the relatively large particle size of the active materials.

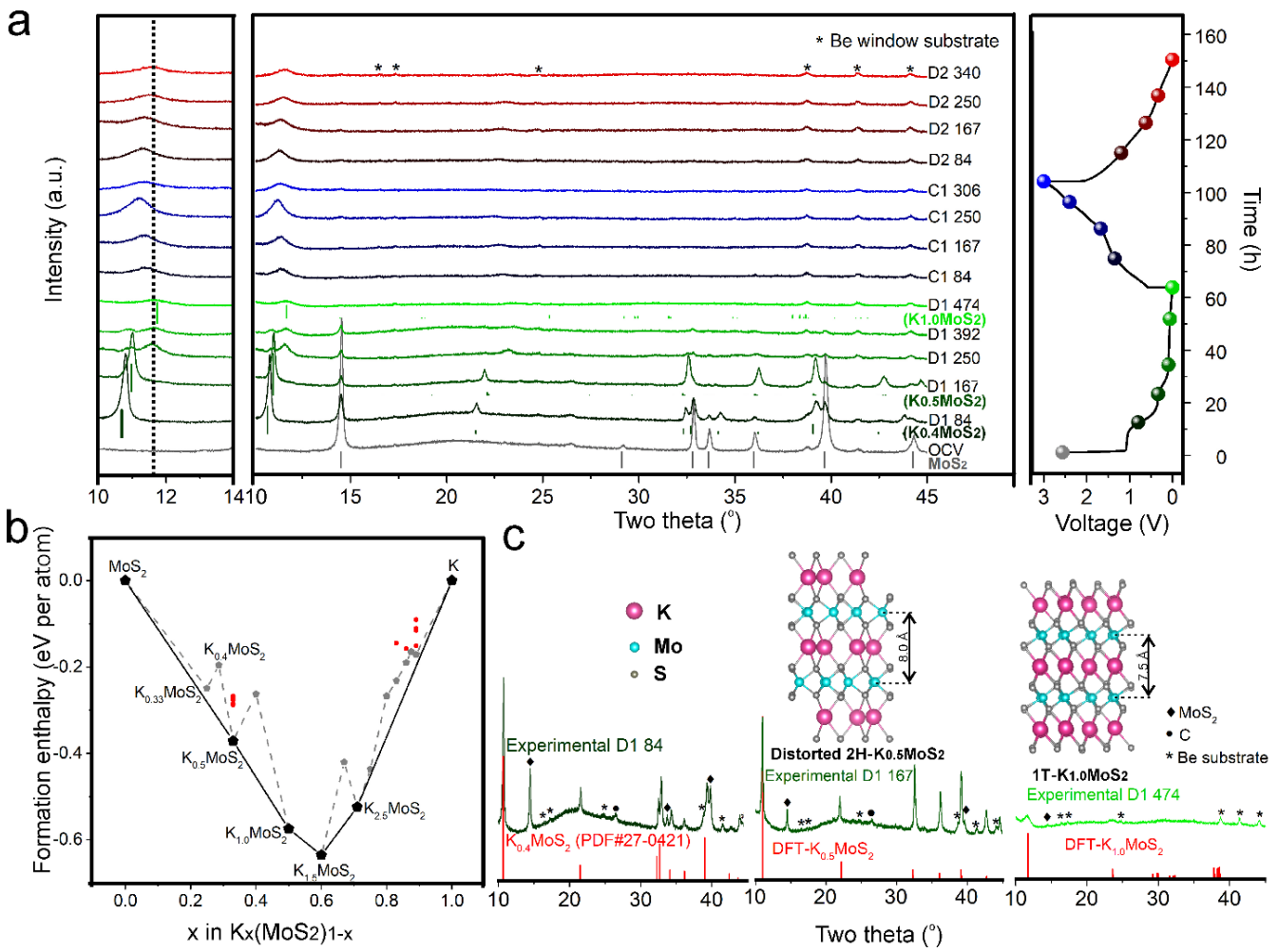

Figure 2 Phase transitions of MoS_2. (a) in situ XRD patterns of MoS_2 at different discharge and charge states, the corresponding voltage profiles are given on the right. For clear visualization, enlarged XRD pattern between 10°-14° is put on the left. The letters stand for first discharge (D1), first charge (C1) and second discharge (D2) with the followed numbers showing the capacity in mA h g^{-1}. (e.g. C1 167 means the capacity is 167 mA h g^{-1} of K ions de-intercalation in the first charge.) (b) Density-functional theory (DFT) calculation with Vdw-optPBE corrections of MoS_2 electrodes. The solid line indicates the thermodynamically stable phases within DFT and temperature errors, while the dashed line refers to the lowest formation enthalpy of each composition. The red dots show the structures in addition to the ones of the lowest enthalpy. (c) The simulated and experimental XRD patterns. Insets are the calculated crystalline structures.

The phase transition is further investigated by in situ Raman. As shown in **Figure 3**, the pristine MoS_2 at OCV condition shows three peaks which can be assigned to E_{1g} (281.3 cm^{-1}), E^1_{2g} (378.2 cm^{-1}) and A_{1g} (404.6 cm^{-1}) vibration model of typical 2H structures. The intensities of E^1_{2g} and A_{1g} peaks decrease with K ion insertion as observed in the D1 84 sample, and finally disappear in the D1 167 sample. Meanwhile, new peaks located at 147 cm^{-1}, 239.2 cm^{-1}, 281.3 $cm^{-1}$and 326.1 cm^{-1}, corresponding to the J_1, J_2, E_{1g} and J_3 of 1T structure, show up and grow along with subsequent K ions insertion. This mainly because 2H-MoS_2 with trigonal phase has been gradually replaced by octahedral 1T-$K_{1.0}MoS_2$ structure, which is consistent with XRD results.[55, 58] At 0 V, the initial 2H phase completely vanishes and only the 1T phase is detected. It is further confirmed with ex-situ test (**Figure S6**). This 1T phase dominates the whole process without recovering to the pristine 2H structure in the following cycles, agrees well with the phase transition between K_xMoS_2 and $K_{1.0}MoS_2$ after first discharge as demonstrated before in XRD tests. The 1T phase, which has different vibration modes with pristine 2H phase, provides high metallic conductivity and ion mobility, low energy unoccupied states for excellent electrochemical performance.[59-62]

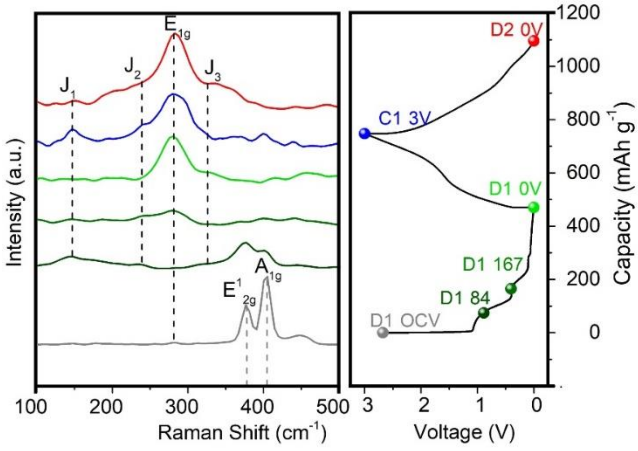

Figure 3 In situ Raman spectra of MoS_2 electrodes at different states and the corresponding voltage profiles.

The combined calculational and experimental results demonstrate that as high as one K ion per MoS_2 could be intercalated instead of 0.4 K ions. Nevertheless, the intercalation behavior could only contribute a capacity of 167 mA h g^{-1}, which is much less than the reversible capacity of 353 mA h g^{-1}. It signifies that conversion reaction must have taken place although the XRD does not show clear traces. We speculate that the conversion products, i.e., Mo and K_2S, have very tiny sizes and probably stay in amorphous states. Therefore, TEM images after different cycles were collected to examine the assumption and probe the morphology evolution of the active materials, as shown in **Figure 4**. The selected area electron diffraction (SAED) and high-resolution transmission electron microscopy (HRTEM) of microsized pristine MoS_2 indicate typical 2H phase and layered structure with d-spacing of 6.1 Å (Figure 4a and b). After discharging to 0 V (Figure 4c and d), the particles remain in microsize instead of breaking up. HRTEM shows that it preserves the layered structure but with an enlarged d-spacing of 7.9 Å, which resembles the $K_{1.0}MoS_2$ phase revealed in XRD. Assisted by the SAED pattern and HRTEM images (insets of Figure 4d, f, and H), metallic Mo (PDF#42-1120) species with the d-spacing of 2.2 Å is discovered with a poor crystallinity.[18] The observations prove that accompanying with intercalation process the conversion reaction $4K+MoS_2 \rightarrow Mo+2K_2S$ also occurs, enabling the detection of metallic Mo. When charging to 3 V, the layered structure is maintained which has similar d-spacing with $K_{1.0}MoS_2$. It does not return to pristine MoS_2 phase, agrees well with in situ XRD tests. The metallic Mo species could still be captured in a charged and cycled sample, reflecting the conversion reaction is not fully reversible (Figure 4e and g). The new ring of 3.5 Å in discharged, charged and cycled samples may be ascribed to K_xS.[63]

Co-occurrence of intercalation and conversion at 0 V is unusual. It differs a lot from previous observations during lithiation and sodiation of MoS_2 in Li- and Na- ion batteries, where all the intercalated compounds will be converted into Mo and Li_2S/Na_xS at a low voltage.[64-65] To further confirm the presence of $K_{1.0}MoS_2$ phase, the fully discharge electrode at 0 V was disassembled and immersed in DI water for one day to remove K ions, which is enlightened by Morrison and co-workers who use forced hydration method to exfoliate MoS_2 from Li_xMoS_2.[66] Interestingly, the phase is recovered to MoS_2 with a clear layered structure, as demonstrated by XRD and TEM in **Figure S7**. Note that it is impossible to restore the MoS_2 phase through oxidation in water if the final reaction products were only Mo and K_2S. Therefore, the intercalated phase $K_{1.0}MoS_2$ must be one of the reaction products at 0 V. Moreover, it is found that only K_xMoS_2 could be obtained during electrochemical oxidation, but a fully de-potassiated MoS_2 is acquired when sinking into water. We suspect that the last de-potassiation step from K_xMoS_2 to MoS_2 has very slow kinetics, deterring the complete extraction of K ions through an electrochemical process. It is partly supported by the fact that short-time rinse with water cannot fully remove K ions. Instead, continuous oxidation as long as one day in the water is required.

Preserve of the layered structure is essential to the integrity of the electrode. To examine the long-term stability, TEM images after 100 cycles are given in Figure 4g and h. It is noted after repeated insertion/extraction, both integrity of the particle and the layered structure are well kept. This is surprising as the volume change arising from conversion and alloy anodes always lead to pulverization of the particles, which is one of the major reasons for their capacity degradation. The unity of the electrode is ascribed to the intercalation behavior of K_xMoS_2, which is intact in the whole process and serves as a framework to avoid the isolation of the particles. To examine the distribution of the intercalation compounds and conversion products, the high-angle annular dark field image (HAADF) in scanning transmission electron microscopy (STEM) and corresponding elements mapping of the samples at first fully discharged, charged and cycled states are shown in Figure 4i, **S8** and **S9**. Mo, S and K elements are uniformly distributed in these samples, signifying the reaction products of intercalation and conversion are interlocking with each other. The schematic of the discharge and charge process is shown in Figure 4j. During the first discharge process, 2H-MoS_2 transfers to 1T-$K_{1.0}MoS_2$ with enlarged interlayer spacing. This broad, rigid construction avoids the huge volume expansion during the K ion intercalation reaction and maintains the structural stability.

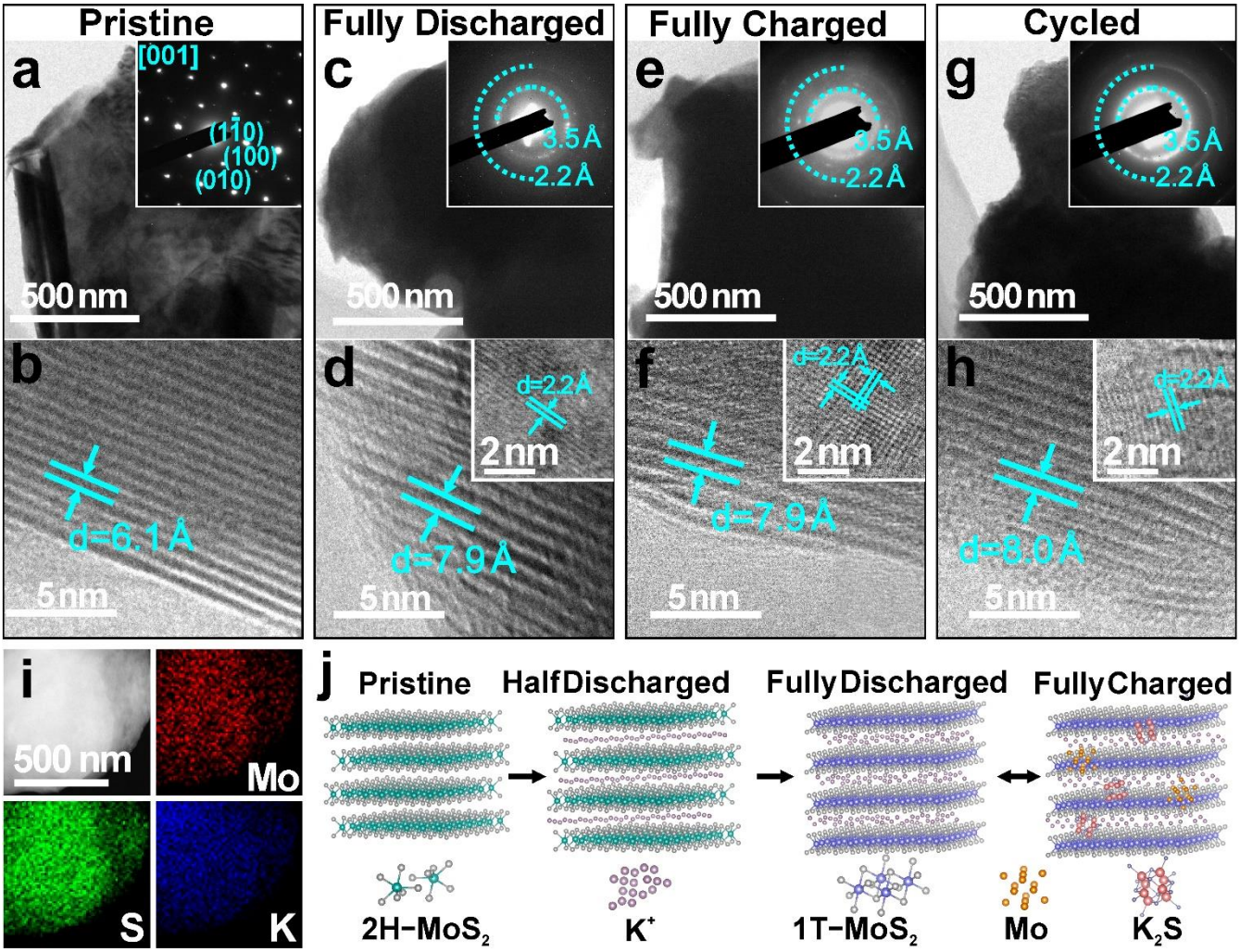

Figure 4 Morphology evolution of MoS_2 electrodes. TEM, corresponding SAED and HRTEM images of (a and b) pristine MoS_2; (c and d) after first discharge to 0 V; (e and f) the first charged to 3V; (g and h) after 100 cycles; Insets: HRTEM image of metallic Mo. (i) HAADF-STEM image and corresponding EDS elemental maps of the first fully discharged MoS_2 electrode; (j) schematic diagram for phase transition of MoS_2.

It is found that the capacity decreases with increasing current densities (**Figure S10**). An intriguing question is how the phase transition is dependent on the current rates. Thus, we collected the ex situ XRD patterns for the electrodes charge/discharged at different current densities, and the results are compared in **Figure 5**a. When cycling at 50 mA g^{-1}, the phase transition process is similar to those observed previously in the in situ tests, where the K ions shuttle between $K_{1.0}MoS_2$ and K_xMoS_2. Once the current density increases to 500 mA g^{-1}, the MoS_2 cannot be fully intercalated but a mixed phases of $K_{0.4}MoS_2$ and $K_{0.5}MoS_2$ are observed. It could be partly recovered to pristine MoS_2 phase in the following charge. With further increasing on the current density to 1000 mA g^{-1}, an even shallower intercalated compound $K_{0.4}MoS_2$ is found at 0 V. The phase is almost fully recovered to MoS_2 in the subsequent charge. The above findings signify a rate dependent phase transition phenomenon in MoS_2. It should be mentioned that the conversion reaction still occurs under all the current rates. Although more conversion is involved under slow rate, the integrity of electrode is also maintained due to the presence of intercalation for stable cycling. The capacity contribution from intercalation and conversion is roughly calculated from the reversible capacities of the electrode and the theoretical capacities of each potassiation path. We suppose all the MoS_2 participated in the reactions. The results are given in the inset of Figure 5b. It can be seen that 63.8% of the total capacity comes from intercalation at a high current rate of 1000 mA g^{-1}, while the value is only 27.5% for the cell tested at 50 mA g^{-1}. The reason lies in the faster kinetics of intercalation than conversion reaction.

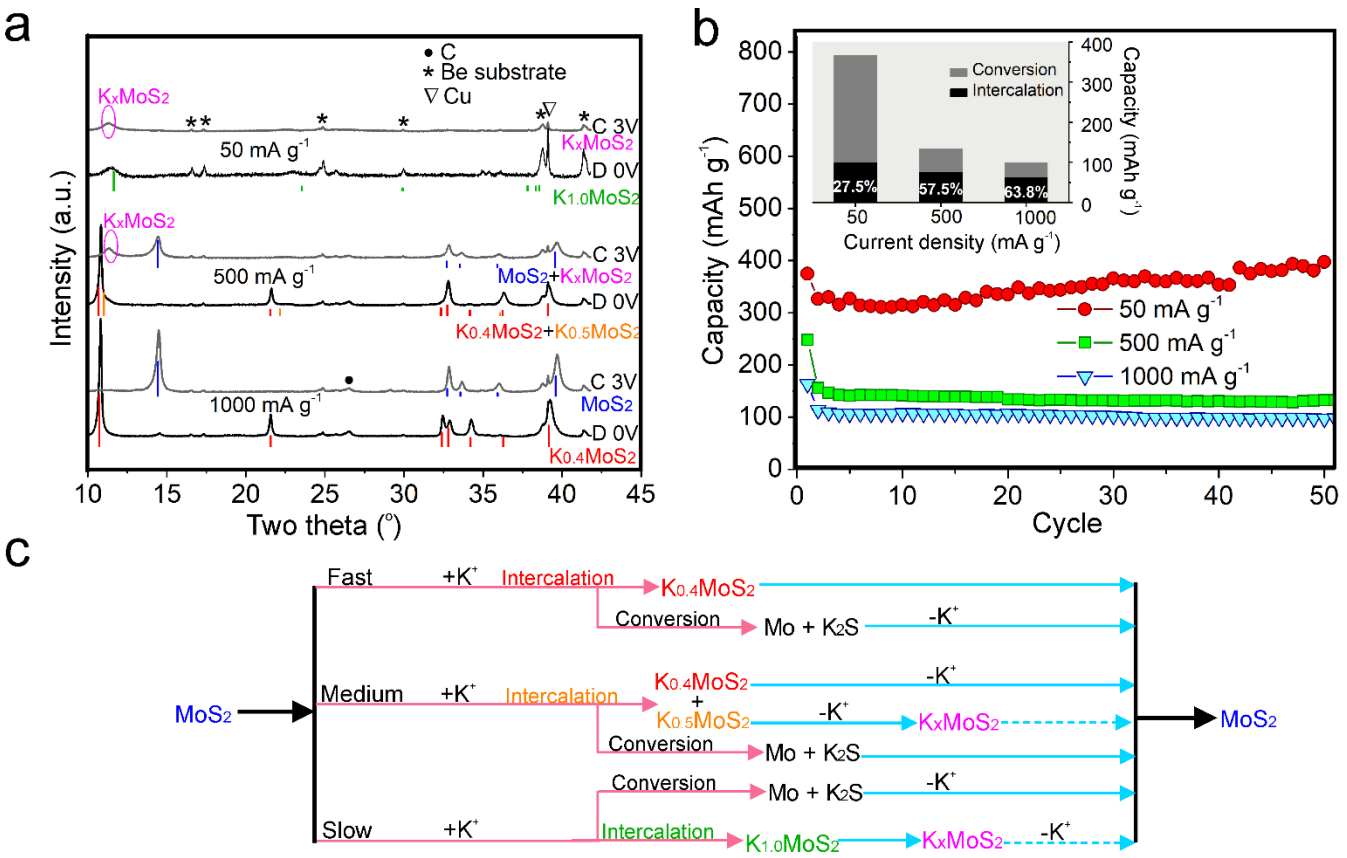

Figure 5 Rate-dependent phase transition. (a) Ex situ XRD pattern of first fully discharged (D 0 V) and charged (C 3 V) MoS_2 electrode with different current density (b) cyclic performance of MoS_2 electrode at different current density (inset: ratio of the capacities contributed by intercalation and conversion); (c) schematic of phase transition for MoS_2 upon K ion insertion. Dash line indicates the process cannot be achieved by electrochemical reaction but is possible through chemical oxidation.

Based on the above discussions, the phase transition of MoS_2 upon potassiation is summarized in Figure 5c. Series intermediate phases are unveiled during K ion intercalation. As many as one K ion could be inserted into MoS_2, differing from 0.4 K ion that reported previously. Nevertheless, the fully potassiated phase only appears when discharging at a low current density. Otherwise a shallow intercalated phase will be observed under a fast discharge. Among the intercalated compounds, only $K_{0.4}MoS_2$ could return to pristine MoS_2 during charge, while the recovery of MoS_2 from K-rich $K_{0.5}MoS_2$ and $K_{1.0}MoS_2$ phases is only possible with chemical oxidation due to slow kinetics. Turning to the conversion reaction, it occurs only after the formation of $K_{0.4}MoS_2$ phase as it is absent when cut-off at 0.5 V in the previous work.[42] The reaction cannot be avoided when discharging to 0 V, no matter at a fast or slow cyclic rate (Fig. Sx), but its contribution to the capacity will be largely reduced with increasing current density. The conversion reaction should be reversible based on the capacity obtained, since single intercalation process would not lead to such a high capacity. The cells deliver stable cyclic performance at both high and low rates (Figure 5b), thanks to the presence of intercalation behaviour, which preserves the layered framework. To make an analogy, the intercalated compounds such as $K_{1.0}MoS_2$ severs as pillars in a house. As long as the pillar stands, the house will not collapse although the inner structure may be destroyed. It explains that a stable capacity of about 360 mA h g^{-1} is obtained under 50 mA g^{-1}, although conversion reaction is involved. The long-term cyclic performance at 1000 mA g^{-1} are presented in **Figure S10**, showing excellent stability with capacity retention of 83% after 300 cycles.

4. Conclusion

In summary, using complementary calculational and experimental methods, we unambiguously reveal the phase transition process of MoS_2 during K ion insertion. Several novel potassium intercalated phases including $K_{0.5}MoS_2$ and $K_{1.0}MoS_2$ are discovered and their detailed crystal structures are unveiled. Instead of fully conversion, which would destroy the layered crystalline structure, the intercalation reaction occurs even being discharged to 0 V. The intercalation compounds inherit the original morphology and play a vital role in maintaining the structural integrity, which prevent the collapse of the particles and result in excellent cyclic stability of microsized MoS_2.

ASSOCIATED CONTENT

Supporting Information. The SEM image of pristine MoS_2, XPS of the electrodes, additional TEM and electrochemical characterizations and calculated lattice parameters, etc. This material is available free of charge via the Internet at http://pubs.acs.org.

AUTHOR INFORMATION

Corresponding Author

*biao.ap.zhang@polyu.edu.hk (Biao Zhang)

Author Contributions

All authors have given approval to the final version of the manuscript. ‡X. D and J. H. contributed equally.

Funding Sources

Hong Kong SAR and the Hong Kong Polytechnic University grant.

Notes

The authors declare no competing financial interest.

ACKNOWLEDGMENT

This work was supported by the General Research Fund through early career scheme (25215918 and 25301617) of Hong Kong SAR and the Hong Kong Polytechnic University grant (Project No. 1-ZE6G).

REFERENCES

1. Jiang, L.; Lu, Y.; Zhao, C.; Liu, L.; Zhang, J.; Zhang, Q.; Shen, X.; Zhao, J.; Yu, X.; Li, H.; Huang, X.; Chen, L.; Hu, Y.-S., Building Aqueous K-ion Batteries for Energy Storage. *Nat. Energy* **2019,** *4*, 495-503.
2. Xu, Y.; Zhang, C.; Zhou, M.; Fu, Q.; Zhao, C.; Wu, M.; Lei, Y., Highly Nitrogen Doped Carbon Nanofibers with Superior Rate Capability and Cyclability for Potassium ion Batteries. *Nat. Commun.* **2018,** *9*, 1720.
3. Wang, J.; Fan, L.; Liu, Z.; Chen, S.; Zhang, Q.; Wang, L.; Yang, H.; Yu, X.; Lu, B., In Situ Alloying Strategy for Exceptional Potassium Ion Batteries. *ACS Nano* **2019,** *13*, 3703-3713.
4. Yao, Y.; Xu, R.; Chen, M.; Cheng, X.; Zeng, S.; Li, D.; Zhou, X.; Wu, X.; Yu, Y., Encapsulation of SeS_2 into Nitrogen-Doped Free-Standing Carbon Nanofiber Film Enabling Long Cycle Life and High Energy Density K-SeS_2 Battery. *ACS Nano* **2019,** *13*, 4695-4704.
5. Jian, Z.; Hwang, S.; Li, Z.; Hernandez, A.S.; Wang, X.; Xing, Z.; Su, D.; Ji, X. Hard–Soft Composite Carbon as a Long- Cycling and High- Rate Anode for Potassium- Ion Batteries. *Adv. Funct. Mater*. **2017**, *27*, 1700324.
6. Zhang, W.; Liu, Y.; Guo, Z. Approaching High-Performance Potassium-ion Batteries via Advanced Design Strategies and Engineering. *Science advances* **2019**, *5*, eaav7412.
7. Kim, H.; Kim, J. C.; Bianchini, M.; Seo, D.-H.; Rodriguez-Garcia, J.; Ceder, G. Recent Progress and Perspective in Electrode Materials for K-Ion Batteries. *Adv. Funct. Mater*. **2018**, *8*, 1702384.
8. Wu, X.; Leonard, D. P.; Ji, X. Emerging Non-Aqueous Potassium-Ion Batteries: Challenges and Opportunities. *Chem. Mater.* **2017**, *29*, 5031-5042.
9. Hwang, J.-Y.; Kim, J.; Yu, T.-Y.; Myung, S.-T.; Sun, Y.-K. Development of P3-$K_{0.69}CrO_2$ as an Ultra-High-Performance Cathode Material for K-Ion Batteries. *Energy Environ. Sci.* **2018**, *11*, 2821-2827.
10. Lin, X.; Huang, J.; Tan, H.; Huang, J.; Zhang, B. $K_3V_2(PO_4)_2F_3$ as a Robust Cathode for Potassium-Ion Batteries. *Energy Storage Mater.* **2019**, *16*, 97-101.
11. Xue, L.; Li, Y.; Gao, H.; Zhou, W.; Lu, X.; Kaveevivitchai, W.; Manthiram, A.; Goodenough, J. B. Low-Cost High-Energy Potassium Cathode. *J. Am. Chem. Soc.* **2017**, *139*, 2164-2167.
12. Pramudita, J. C.; Sehrawat, D.; Goonetilleke, D.; Sharma, N. An Initial Review of the Status of Electrode Materials for Potassium-Ion Batteries. *Adv. Energy Mater.* **2017**, *7*, 1602911.
13. Sultana, I.; Rahman, M. M.; Chen, Y.; Glushenkov, A. M., Potassium-Ion Battery Anode Materials Operating through the Alloying-Dealloying Reaction Mechanism. *Adv. Funct. Mater*. **2018**, *28*, 1703857.
14. Jian, Z.; Luo, W.; Ji, X. Carbon Electrodes for K-Ion Batteries. *J. Am. Chem. Soc.* **2015**, *137*, 11566-11569.
15. Kishore, B.; Venkatesh, G.; Munichandraiah, N. $K_2Ti_4O_9$: A Promising Anode Material for Potassium Ion Batteries. *J. Electrochem. Soc.* **2016**, *163*, A2551-A2554.
16. Huang, J. Q.; Lin, X. Y.; Tan, H.; Zhang, B. Bismuth Microparticles as Advanced Anodes for Potassium-Ion Battery. *Adv. Energy Mater*. **2018**, *8*, 1703496.
17. Zheng, J.; Yang, Y.; Fan, X.; Ji, G.; Ji, X.; Wang, H.; Hou, S.; Zachariah, M. R.; Wang, C., Extremely Stable Antimony–Carbon Composite Anodes for Potassium-ion Batteries. *Energy Environ. Sci.* **2019,** *12*, 615-623.
18. Jia, B.; Yu, Q.; Zhao, Y.; Qin, M.; Wang, W.; Liu, Z.; Lao, C.Y.; Liu, Y.; Wu, H.; Zhang, Z.; Qu, X. Bamboo-Like Hollow Tubes with MoS_2/N-Doped-C Interfaces Boost Potassium-Ion Storage. *Adv. Funct. Mater.* **2018**, *28*, 1803409.
19. Lei, K.; Wang, C.; Liu, L.; Luo, Y.; Mu, C.; Li, F.; Chen, J. A Porous Network of Bismuth Used as the Anode Material for High-Energy-Density Potassium-Ion Batteries. *Angew. Chem. Int. Ed. Engl.* **2018**, *57*, 4687-4691.
20. Luo, Z.; Zhou, J.; Wang, L.; Fang, G.; Pan, A.; Liang, S., Two-Dimensional Hybrid Nanosheets of Few Layered $MoSe_2$ on Reduced Graphene Oxide as Anodes for Long-Cycle-Life Lithium-Ion Batteries. *J. Mater. Chem. A* **2016,** *4*, 15302-15308.
21. Ge, J.; Fan, L.; Wang, J.; Zhang, Q.; Liu, Z.; Zhang, E.; Liu, Q.; Yu, X.; Lu, B., $MoSe_2$/N-Doped Carbon as Anodes for Potassium-Ion Batteries. *Adv. Energy Mater*. **2018,** *8*, 1801477.
22. Wang, W.; Jiang, B.; Qian, C.; Lv, F.; Feng, J.; Zhou, J.; Wang, K.; Yang, C.; Yang, Y.; Guo, S. Pistachio-Shuck-Like $MoSe_2$/C Core/Shell Nanostructures for High-Performance Potassium-Ion Storage. *Adv. Mater*. **2018**, *30*, 1801812.
23. Jia, B.; Zhao, Y.; Qin, M.; Wang, W.; Liu, Z.; Lao, C.-Y.; Yu, Q.; Liu, Y.; Wu, H.; Zhang, Z.; Qu, X., Multirole Organic-Induced Scalable Synthesis of a Mesoporous MoS_2-Monolayer/Carbon Composite for High-Performance Lithium and Potassium Storage. *J. Mater. Chem. A* **2018,** *6*, 11147-11153.
24. Xie, K.; Yuan, K.; Li, X.; Lu, W.; Shen, C.; Liang, C.; Vajtai, R.; Ajayan, P.; Wei, B. Superior Potassium Ion Storage Via Vertical MoS_2 "Nano-Rose" with Expanded Interlayers on Graphene. *Small* **2017**, *13*, 1701471.
25. Tian, B.; Tang, W.; Leng, K.; Chen, Z.; Tan, S. J. R.; Peng, C.; Ning, G.-H.; Fu, W.; Su, C.; Zheng, G. W.; Loh, K. P., Phase Transformations in TiS_2 during K Intercalation. *ACS Energy Lett.* **2017,** *2*, 1835-1840.
26. Yang, C.; Feng, J.; Lv, F.; Zhou, J.; Lin, C.; Wang, K.; Zhang, Y.; Yang, Y.; Wang, W.; Li, J.; Guo, S., Metallic Graphene-Like VSe_2 Ultrathin Nanosheets: Superior Potassium-Ion Storage and Their Working Mechanism. *Adv Mater* **2018,** *30*, 1800036.
27. Mao, M.; Cui, C.; Wu, M.; Zhang, M.; Gao, T.; Fan, X.; Chen, J.; Wang, T.; Ma, J.; Wang, C., Flexible ReS_2 Nanosheets/N-doped Carbon Nanofibers-Based Paper as a Universal Anode for Alkali (Li, Na, K) Ion Battery. *Nano Energy* **2018,** *45*, 346-352.
28. Wang, Y.; Wang, Z.; Chen, Y.; Zhang, H.; Yousaf, M.; Wu, H.; Zou, M.; Cao, A.; Han, R. P. S., Hyperporous Sponge Interconnected by Hierarchical Carbon Nanotubes as a High-Performance Potassium-Ion Battery Anode. *Adv Mater* **2018,** *30*, 1802074.
29. Liu, L.; Chen, Y.; Xie, Y.; Tao, P.; Li, Q.; Yan, C. Understanding of the Ultrastable K-Ion Storage of Carbonaceous Anode. *Adv. Funct. Mater.* **2018**, *28*, 1801989.
30. Bin, D. S.; Lin, X. J.; Sun, Y. G.; Xu, Y. S.; Zhang, K.; Cao, A. M.; Wan, L. J. Engineering Hollow Carbon Architecture for High-Performance K-Ion Battery Anode. *J. Am. Chem. Soc.* **2018**, *140*, 7127-7134.

31. Cao, B.; Zhang, Q.; Liu, H.; Xu, B.; Zhang, S.; Zhou, T.; Mao, J.; Pang, W.K.; Guo, Z.; Li, A.; Zhou, J. Graphitic Carbon Nanocage as a Stable and High Power Anode for Potassium-Ion Batteries. *Adv. Energy Mater.* **2018**, *8*, 1801149.
32. Chen, Z.; Yin, D.; Zhang, M., Sandwich-like MoS_2@SnO_2@C with High Capacity and Stability for Sodium/Potassium Ion Batteries. *Small* **2018,** *14*, 1703818.
33. Zhang, J.; Wang, D.-W.; Lv, W.; Zhang, S.; Liang, Q.; Zheng, D.; Kang, F.; Yang, Q.-H. Achieving Superb Sodium Storage Performance on Carbon Anodes through an Ether-Derived Solid Electrolyte Interphase. *Energy Environ. Sci.* **2017**, *10*, 370-376.
34. Soto, F.A.; Yan, P.; Engelhard, M.H.; Marzouk, A.; Wang, C.; Xu, G.; Chen, Z.; Amine, K.; Liu, J.; Sprenkle, V.L.; El-Mellouhi, F. Tuning the Solid Electrolyte Interphase for Selective Li- and Na-Ion Storage in Hard Carbon. *Adv. Mater.* **2017**, *29*, 1606860.
35. Li, K.; Zhang, J.; Lin, D.; Wang, D. W.; Li, B.; Lv, W.; Sun, S.; He, Y. B.; Kang, F.; Yang, Q. H.; Zhou, L.; Zhang, T. Y., Evolution of the Electrochemical Interface in Sodium Ion Batteries with Ether Electrolytes. *Nat. Commun.* **2019,** *10*, 725.
36. Huang, J.; Guo, X.; Du, X.; Lin, X.; Huang, J.-Q.; Tan, H.; Zhu, Y.; Zhang, B., Nanostructures of Solid Electrolyte Interphases and Their Consequences for Microsized Sn Anodes in Sodium Ion Batteries. *Energy Environ. Sci.* **2019,** *12*, 1550-1557.
37. Zhang, B.; Rousse, G.; Foix, D.; Dugas, R.; Corte, D. A.; Tarascon, J. M. Microsized Sn as Advanced Anodes in Glyme-Based Electrolyte for Na-Ion Batteries. *Adv. Mater.* **2016**, *28*, 9824-9830.
38. Wang, C.; Wang, L.; Li, F.; Cheng, F.; Chen, J. Bulk Bismuth as a High-Capacity and Ultralong Cycle-Life Anode for Sodium-Ion Batteries by Coupling with Glyme-Based Electrolytes. *Adv. Mater.* **2017**, *29*, 1702212.
39. Zhang, J.; Wang, D.-W.; Lv, W.; Qin, L.; Niu, S.; Zhang, S.; Cao, T.; Kang, F.; Yang, Q.-H. Ethers Illume Sodium-Based Battery Chemistry: Uniqueness, Surprise, and Challenges. *Adv. Energy Mater.* **2018**, *8*, 1801361.
40. Yang, E.; Ji, H.; Jung, Y., Two-Dimensional Transition Metal Dichalcogenide Monolayers as Promising Sodium Ion Battery Anodes. *J. Phys. Chem. C* **2015,** *119*, 26374-26380.
41. Wang, H.; Wang, X.; Wang, L.; Wang, J.; Jiang, D.; Li, G.; Zhang, Y.; Zhong, H.; Jiang, Y., Phase Transition Mechanism and Electrochemical Properties of Nanocrystalline $MoSe_2$ as Anode Materials for the High Performance Lithium-Ion Battery. *J. Phys. Chem. C* **2015,** *119*, 10197-10205.
42. Chong, S.; Sun, L.; Shu, C.; Guo, S.; Liu, Y.; Wang, W.; Liu, H. K., Chemical Bonding Boosts Nano-Rose-Like MoS_2 Anchored on Reduced Graphene Oxide for Superior Potassium-Ion Storage. *Nano Energy* **2019**, *63*.
43. Ren, X.; Zhao, Q.; McCulloch, W. D.; Wu, Y., MoS_2 as a Long-Life Host Material for Potassium Ion Intercalation. *Nano Research* **2017,** *10*, 1313-1321.
44. Blöchl, P. E. Projector Augmented-Wave Method. *Physical Review B* **1994**, *50*, 17953-17979.
45. Kresse, G.; Furthmüller, J. Efficient Iterative Schemes for Ab Initio Total-Energy Calculations Using a Plane-Wave Basis Set. *Physical review B* **1996**, *54*, 11169-11186.
46. Perdew, J. P.; Burke, K.; Ernzerhof, M. Generalized Gradient Approximation Made Simple. *Physical review letters* **1996**, *77*, 3865-3868.
47. Klimes, J.; Bowler, D. R.; Michaelides, A. Chemical Accuracy for the Van Der Waals Density Functional. *J. Phys. Condens. Matter.* **2010**, *22*, 022201.
48. Xiao, Y.; Miara, L. J.; Wang, Y.; Ceder, G., Computational Screening of Cathode Coatings for Solid-State Batteries. *Joule* **2019**, *3*, 1252-1275.
49. Zhang, Q.; Mao, J.; Pang, W. K.; Zheng, T.; Sencadas, V.; Chen, Y.; Liu, Y.; Guo, Z. Boosting the Potassium Storage Performance of Alloy-Based Anode Materials Via Electrolyte Salt Chemistry. *Adv. Energy Mater.* **2018**, *8*, 1703288.
50. Xiao, N.; McCulloch, W. D.; Wu, Y., Reversible Dendrite-Free Potassium Plating and Stripping Electrochemistry for Potassium Secondary Batteries. *J. Am. Chem. Soc.* **2017,** *139*, 9475-9478.
51. Li, Y.; Liang, Y.; Robles Hernandez, F. C.; Deog Yoo, H.; An, Q.; Yao, Y. Enhancing Sodium-Ion Battery Performance with Interlayer-Expanded MoS_2-PEO Nanocomposites. *Nano Energy* **2015**, *15*, 453-461.
52. Zhang, R.; Tsai, I. L.; Chapman, J.; Khestanova, E.; Waters, J.; Grigorieva, I. V. Superconductivity in Potassium-Doped Metallic Polymorphs of MoS_2. *Nano Lett.* **2016**, *16*, 629-636.
53. Gao, P.; Wang, L.; Zhang, Y.; Huang, Y.; Liu, K. Atomic-Scale Probing of the Dynamics of Sodium Transport and Intercalation-Induced Phase Transformations in MoS_2. *ACS Nano* **2015**, *9*, 11296-11301.
54. Xie, X.; Makaryan, T.; Zhao, M.; Van Aken, K. L.; Gogotsi, Y.; Wang, G. MoS_2 Nanosheets Vertically Aligned on Carbon Paper: A Freestanding Electrode for Highly Reversible Sodium-Ion Batteries. *Adv. Energy Mater.* **2016**, *6*, 1502161.
55. Zhang, L.; Sun, D.; Kang, J.; Feng, J.; Bechtel, H. A.; Wang, L. W.; Cairns, E. J.; Guo, J. Electrochemical Reaction Mechanism of the MoS_2 Electrode in a Lithium-Ion Cell Revealed by in Situ and Operando X-Ray Absorption Spectroscopy. *Nano Lett.* **2018**, *18*, 1466-1475.
56. George, C.; Morris, A. J.; Modarres, M. H.; De Volder, M. Structural Evolution of Electrochemically Lithiated MoS_2 Nanosheets and the Role of Carbon Additive in Li-Ion Batteries. *Chem. Mater.* **2016**, *28*, 7304-7310.
57. Andersen, A.; Kathmann, S. M.; Lilga, M. A.; Albrecht, K. O.; Hallen, R. T.; Mei, D. First-Principles Characterization of Potassium Intercalation in Hexagonal 2h-MoS_2. *J. Phys. Chem. C* **2012**, *116*, 1826-1832.
58. Leng, K.; Chen, Z.; Zhao, X.; Tang, W.; Tian, B.; Nai, C. T.; Zhou, W.; Loh, K. P. Phase Restructuring in Transition Metal Dichalcogenides for Highly Stable Energy Storage. *ACS Nano* **2016**, *10*, 9208-9215.
59. Acerce, M.; Voiry, D.; Chhowalla, M., Metallic 1T Phase MoS_2 Nanosheets as Supercapacitor Electrode Materials. *Nat. Nanotechnol.* **2015**, *10*, 313-318.
60. Jiao, Y.; Hafez, A. M.; Cao, D.; Mukhopadhyay, A.; Ma, Y.; Zhu, H., Metallic MoS_2 for High Performance Energy Storage and Energy Conversion. *Small* **2018**, *14*, 1800640.
61. Shu, H.; Li, F.; Hu, C.; Liang, P.; Cao, D.; Chen, X., The Capacity Fading Mechanism and Improvement of Cycling Stability in Mos2-Based Anode Materials for Lithium-Ion Batteries. *Nanoscale* **2016**, *8*, 2918-2926.
62. Sun, D.; Huang, D.; Wang, H.; Xu, G.L.; Zhang, X.; Zhang, R.; Tang, Y.; EI-Hady, D.A.; Alshitari, W.; AL-Bogami, A.S.; Amine, K. 1T MoS_2 Nanosheets with Extraordinary Sodium Storage Properties Via Thermal-Driven Ion Intercalation Assisted Exfoliation of Bulky MoS_2. *Nano Energy* **2019**, *61*, 361-369.
63. Zhao, Q.; Hu, Y.; Zhang, K.; Chen, J., Potassium-Sulfur Batteries: A New Member of Room-Temperature Rechargeable Metal-Sulfur Batteries. *Inorg. Chem* **2014**, *53*, 9000-9005.
64. Stephenson, T.; Li, Z.; Olsen, B.; Mitlin, D. Lithium Ion Battery Applications of Molybdenum Disulfide (MoS_2) Nanocomposites. *Energy Environ. Sci.* **2014**, *7*, 209-231.
65. Wang, X. F.; Shen, X.; Wang, Z. X.; Yu, R. C.; Chen, L. Q. Atomic-Scale Clarification of Structural Transition of MoS_2 Upon Sodium Intercalation. *ACS Nano* **2014**, *8*, 11394-11400.
66. Joensen, P.; Frindt, R.; Morrison, S. R. Single-Layer MoS_2. *Mat. Res. Bull.* **1986**, *21*, 457-461.

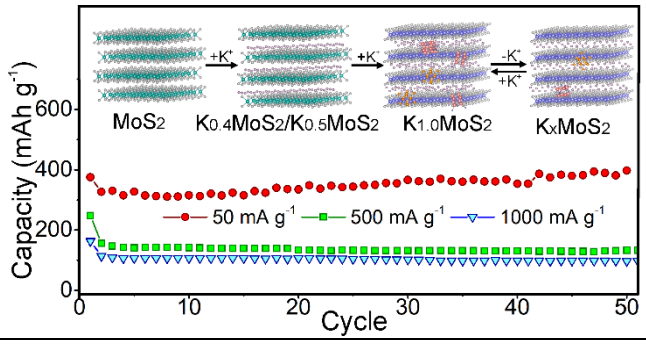
MoS2
K0.4MoS2/K0.5MoS2
K1.0MoS2
KxMoS2
+K+
+K+
-K+
+K+
Capacity (mAh g-1)
Cycle
50 mA g-1
500 mA g-1
1000 mA g-1
0
200
400
600
0
10
20
30
40
50